



Fluoride removal performance of highly porous activated alumina

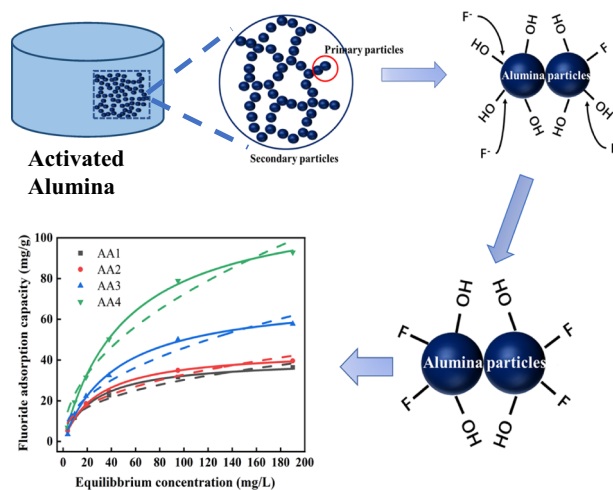
Chenglong Yu¹ · Lin Liu¹ · Xiaodong Wang¹ · Jiarui Fu² · Yinan Wu² · Chen Feng¹ · Yu Wu¹ · Jun Shen¹

Received: 19 May 2021 / Accepted: 28 December 2021 / Published online: 9 February 2022
© The Author(s), under exclusive licence to Springer Science+Business Media, LLC, part of Springer Nature 2022

Abstract

Activated alumina (AA) with metastable crystal phase and porous structure has shown great potential for fluoride ion removal. Conventional AA is obtained by direct calcination, which limits its fluoride adsorption ability due to the low surface area and limited active sites. In this work, a highly porous AA was synthesized by a sol-gel method, followed with supercritical drying (including ethanol supercritical drying and carbon dioxide supercritical drying) and calcination. The fluoride ion adsorption properties of AA were studied at different concentrations of fluoride in solution. The Langmuir model, Freundlich model, pseudo-first-order model and pseudo-second-order model were used to describe the adsorption process. The results show that the resulting AAs possess a high porosity and a high specific surface area (up to 660 m²/g). The fluoride adsorption capacity of AA increases with the increase of specific surface area and porosity (up to 119.2 mg/g), which is much higher than that of AA prepared by the traditional method (direct calcination). Moreover, all the fitted correlation coefficients of the four models exceed 90%, indicating both chemical and physical adsorption in AA.

Graphical abstract



These authors contributed equally: Chenglong Yu, Lin Liu

✉ Xiaodong Wang
xiaodong_wang@tongji.edu.cn

✉ Jun Shen
shenjun67@tongji.edu.cn

Materials and Technology, School of Physics Science and Engineering, Tongji University, Shanghai 200092, PR China

² College of Environmental Science and Engineering, State Key Laboratory of Pollution Control and Resource Reuse, Tongji University, Shanghai 200092, PR China

¹ Shanghai Key Laboratory of Special Artificial Microstructure

Keywords Activated alumina · Sol–gel · Supercritical drying · Adsorption of fluoride ions.

Highlights

- Activated alumina (AA) was prepared by sol–gel method, followed with supercritical drying.
- The highest fluoride adsorption capacity of porous AA is 119.2 mg/g.
- The number of active sites of AA increases due to the high porosity and specific surface area.

1 Introduction

Fluorine is one of the essential trace elements for the human body, but excessive fluoride could damage human teeth and bones, which is harmful to human health [1]. The fluoride content in the drinking water of more than 200 million people in the world exceeds the guidelines set by the World Health Organization (WHO) [2]. In the natural environment, rocks and minerals discharge fluoride into groundwater through long-term weathering [3, 4]. Besides, man-made sources are also the main factor for fluoride pollution. For instance, in the semiconductor manufacturing industry, the use of hydrofluoric acid will produce a large amount of fluoride-containing wastewater [5, 6]. Various methods including precipitation, adsorption, reverse osmosis, electrocoagulation and ion exchange [7–12] have been developed to solve the problem of fluoride-containing wastewater. Due to its good fluoride removal ability, simple procedure and low cost, the adsorption method has become the most commonly used method for fluoride removal [13]. At present, the commonly used adsorbents are activated carbon, calcite, activated alumina (AA), hydroxyapatite, and fly ash [14]. Granular AA with γ crystal phase possesses a porous structure and large specific surface area, and has been widely used for the adsorption of fluoride ions [15, 16]. Xu et al. [17] prepared mesoporous γ -alumina with ordered wormhole-like mesoporous structure by a facile hydrothermal method for fluoride removal. Such γ -Al₂O₃ exhibits an average crystallite size of 20–150 nm and high specific surface area, which can greatly improve the adsorption capacity of F⁻. By modification with calcium oxide or manganese oxide [18], alum [19], ionic liquid [20], hydroxyapatite [21], and magnetic Fe₃O₄ [22, 23], the fluoride removal efficiency of AA could be enhanced. In order to further improve the fluoride adsorption performance, many methods have been developed to prepare AA with high specific surface area. For instance, organic acids were added during the gelation process

to increase its specific surface area after calcination [13]. Polyhollow alumina spheres were prepared via a facile ball dropping method based on particle-stabilized emulsions, which can still maintain hierarchical pore structure and high surface area at 400–900 °C [24]. Shi et al. [25] fabricated hierarchically structured boehmite with a flower-like morphology that have small particle size and large surface area. However, the AA obtained by calcination still has few active sites due to the low specific surface area, which also limits its adsorption capacity. Therefore, it is imperative to synthesize AA with a higher specific surface area for better fluoride adsorption performance. In this work, we prepared AA with higher porosity and higher specific surface area by a supercritical drying method without using any chelating agents. The resulting AA exhibits better fluoride ion adsorption performance compared to previous works. The effect of specific surface area and porosity on its fluoride ion adsorption capacity was studied through comparing the fluoride ion adsorption performance of the AA obtained by different drying methods.

2 Experimental section

2.1 Materials

Ethanol (EtOH, 99%), sodium fluoride, distilled water, and AlCl₃·6H₂O (99%) were purchased from Sinopharm Chemical Reagent Corporation (China). Aluminum secbutoxide (ASB, 97%) was obtained from Zhejiang Ultrafine Powders & Chemicals Corporation (China). All of the chemical reagents were used as received.

2.2 Sample preparation

Different types of AAs were prepared by sol–gel methods followed with different drying methods and calcination.

Table 1 Preparation condition of different samples

Sample	Drying method	Calcination temperature
AA1	Ambient drying at room temperature	500 °C
AA2	Ambient drying at 60 °C	500 °C
AA3	Carbon dioxide supercritical drying	500 °C
AA4	Ethanol supercritical drying	500 °C

ASB (5 g, 20.3 mmol) was dissolved in a mixed solution of 15 ml EtOH and 0.2 ml deionized water, and stirred at 70 °C to obtain a transparent alumina sol. After dissolving of $\text{AlCl}_3 \cdot 6\text{H}_2\text{O}$ (4.35 g, 18.1 mmol) in 5 mL of absolute EtOH, it was slowly poured into the previous alumina sol. The mixed sol usually forms a gel within 10 min. The gel was aged for 2 days followed by washing with ethanol for 4 times (every 12 h). After aging and replacing of the solvent, the gel was dried with four different methods to obtain different types of alumina. The dried sample was finally calcined at 500 °C for 2 h to obtain activated γ alumina. As shown in Table 1, the sample obtained by ambient drying at room temperature was named as AA1, while that dried at 60 °C was named as AA2. The samples dried by carbon dioxide supercritical drying and ethanol supercritical drying were denoted as AA3 and AA4, respectively.

2.3 Characterization

The morphology and energy dispersive X-ray spectroscopy (EDS) mapping of AA samples were characterized by scanning electron microscopy (SEM, Philips XL30FEG, The Netherlands). The crystal phase of AA samples was analyzed with powder X-ray diffraction (XRD) in a Rigata/max-C diffractometer using $\text{Cu-K}\alpha$ radiation (DX-2700, Hao Yuan Instrument, China). The specific surface area, pore volume and pore-size distribution were determined by the Brunauer–Emmett–Teller (BET) and Barrett–Joyner–Halenda (BJH) methods using an Autosorb iQ analyzer (Quantachrome Instruments) through nitrogen adsorption/desorption. Fluoride ion selective electrode PF-2-01 (Leici, China) was used to determine the fluoride concentration in aqueous solution.

2.4 Fluoride ion adsorption test

To study the fluoride ion adsorption performance of AAs, 30 mg of adsorbent was added into 100 mL sodium fluoride solution with different F^- concentration (3.8, 9.5, 19, 38, 95, and 190 mg/L). The mixed suspension was then shaken at 25 °C with a shaking speed of 100 rpm. After stirring for 48 h, the solid and liquid were separated and the supernatants were detected by fluoride ion selective electrode (PF-2-01) to calculate the fluoride ion concentration. During the entire test, the pH of the solution was kept at 5.0 by manually adjusting with 0.01 mol/L HCl and NaOH every 2 h.

The Langmuir and Freundlich models were used to describe the adsorption isotherm data [26, 27]. The Langmuir isotherm equation is given below:

$$q_e = \frac{q_{\max} b C_e}{1 + b C_e} \quad (1)$$

where C_e (mg/L) is the fluoride ion concentration at equilibrium, q_e (mg/g) is the fluoride ions adsorbed per gram of the adsorbent at equilibrium, q_{\max} (mg/g) is the maximum adsorption capacity, and b (L/mg) is the Langmuir constant.

The nonuniform distribution of heat of adsorption over the heterogeneous surface is represented by the Freundlich isotherm with the following equation:

$$q_e = k C_e^{1/n} \quad (2)$$

where K and $1/n$ are the Freundlich constant and the heterogeneity factor, respectively. To describe the adsorption kinetic characteristic, 30 mg of adsorbent was added into 100 mL sodium fluoride solution with F^- concentration of 38 mg/L. The fluoride ion concentration of the solution was then determined using the fluoride ion selective electrode at different time points (5, 15, 30, 60, 240, 720, and 1440 min). The pseudo-first-order and pseudo-second-order kinetic models were used to describe the kinetic data:

$$\text{pseudo - first - order model : } \ln(Q_e - Q_t) = \ln Q_e - k_1 t \quad (3)$$

$$\text{pseudo - second - order model : } t/Q_t = 1/k_2 Q_e^2 + t/Q_e \quad (4)$$

where Q_e is the equilibrium adsorption capacity, Q_t is the adsorption capacity at time t , and k_1 and k_2 are rate constants of the pseudo-first-order model and pseudo-second-order model, respectively.

3 Results and discussion

3.1 Structure and composition characterization

The XRD patterns of the samples are given in Fig. 1a. After heat treatment at 500 °C, AA displays diffuse diffraction peaks at $2\theta = 37.7, 45.9$ and 67° , corresponding to the diffraction peaks of $\gamma\text{-Al}_2\text{O}_3$ (311), (400) and (440) crystal planes (PDF no.10-0425) [28, 29]. These three diffraction peaks are clearly resolved in all the 500 °C calcined samples, which indicates that all samples were converted into $\gamma\text{-Al}_2\text{O}_3$ after calcination at 500 °C. Figure 1b shows the FTIR spectra of the AA samples. The absorbance peaks at 3451 and 1637 cm^{-1} correspond to the stretching and bending vibrations of physically adsorbed water, respectively [30]. The peak at 1428 cm^{-1} corresponds to the vibration of C–H [31], while the peak at 599 cm^{-1} is ascribed to the stretching vibration of Al–O–Al [31]. $\gamma\text{-Al}_2\text{O}_3$ is a defective spinel structure consisting of AlO_6 octahedron, AlO_4 tetrahedron

Fig. 1 **a** XRD patterns and **b** FTIR spectra of AA samples

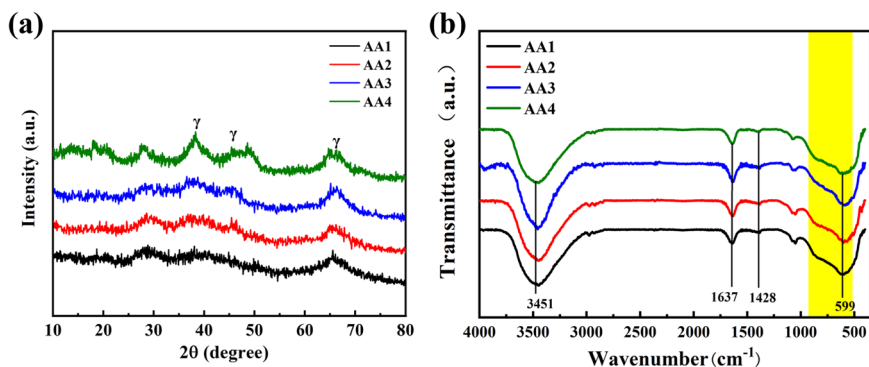
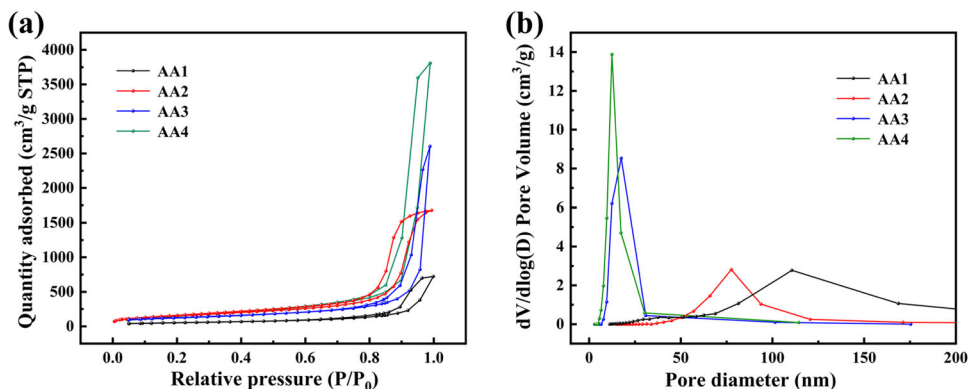


Fig. 2 **a** Nitrogen adsorption–desorption isotherms of AA samples; **b** Pore-size distribution curves of the of AA samples



and vacancy defects. The broad absorption band at 500–950 cm^{-1} (the highlighted part in Fig. 2b) is attributed to the torsional vibration, stretching vibration, and bending vibrations of Al–O bonds, which suggests the presence of oxygen vacancies around Al^{3+} and a disordered arrangement [32]. XRD and FTIR results confirm that the crystalline phase of the four AA samples calcined at 500 $^{\circ}\text{C}$ are $\gamma\text{-Al}_2\text{O}_3$.

Figure 2 shows the nitrogen adsorption/desorption isotherms of AA samples. According to the classification method of the International Union of Pure and Applied Chemistry, the isothermal adsorption/desorption curves of AAs correspond to type IV, which is characteristic of mesoporous materials. AA1 and AA2 exhibit H1 hysteresis loop in the relative pressure range of 0.8–1.0, indicating that AA1 and AA2 are mainly formed by the uniform agglomerated nanoparticles. AA3 and AA4 display H3 hysteresis loop, which suggests that the pores of AA3 and AA4 are composed of slit shaped nanopores [33]. The pore-size distribution curve was calculated using the BJH method from the desorption isotherm and is given in Fig. 2b. The pore-size distribution of supercritical dried samples AA3 and AA4 are mainly concentrated in range of 10–20 nm, while the pore size of the ambient pressure dried samples AA1 and AA2 are larger than 50 nm. This indicates that a more mesoporous structure can be obtained by using the supercritical drying method. The calculated pore structure parameters of the AA samples are listed in Table 2. It is

Table 2 Pore structure parameters of AA samples

Sample	$S_{\text{BET}}^{\text{a}}$ (m^2/g)	D^{b} (nm)	V^{c} (cm^3/g)
AA1	187	105.4	0.68
AA2	219	72.3	1.88
AA3	489	23.5	2.65
AA4	660	12.9	4.03

^aBET specific surface area

^bAverage pore diameter obtained from nitrogen desorption branch by BJH method

^cTotal pore volume

noticeable that the specific surface area and pore volume of the AAs obtained by supercritical drying methods are much higher than those of the AAs obtained by ambient pressure drying (AA1 and AA2). Sample AA4 that was dried by ethanol supercritical drying possess the highest specific surface area of 660 m^2/g and the largest pore volume of 4.03 cm^3/g , which is 3.5 times and 5.9 times higher than those of AA1, respectively. This is due to the large shrinkage and collapse of the skeleton of the sample during ambient pressure drying [34]. In contrast, the supercritical drying process can convert the liquid inside the gel into fluid and then exhaust it, which avoids capillary force and maintains the pore structure inside the gel [35].

Figure 3 shows the SEM images of AA obtained by different drying methods. The room temperature dried AA1

Fig. 3 SEM images of AA samples: **a** AA1, **b** AA2, **c** AA3, and **d** AA4

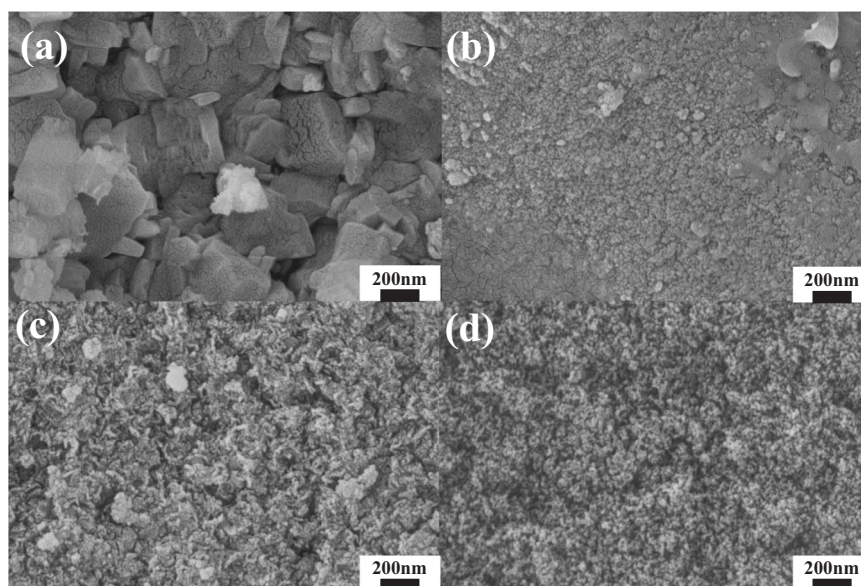


Fig. 4 **a** F^- adsorption isotherms of different AA samples. (solid lines: Langmuir model; dotted lines: Freundlich model); **b** F^- adsorption kinetic data of AA samples. (solid lines: pseudo-first-order model; dotted lines: pseudo-second-order model)

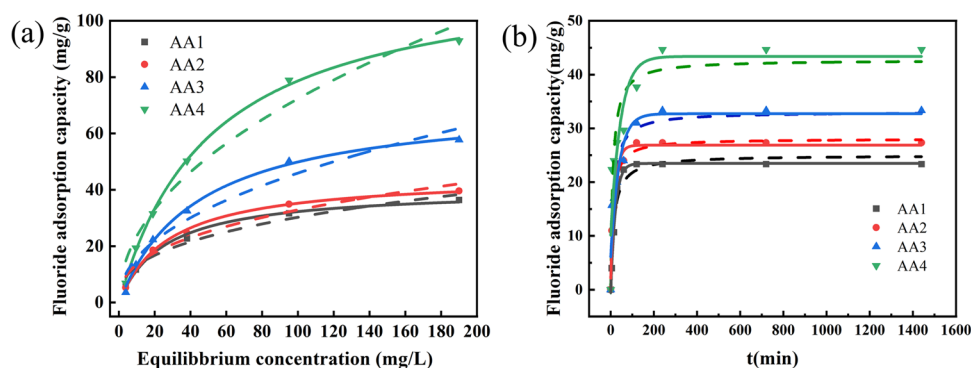


Table 3 Adsorption isotherm parameters for F^- adsorption of AA samples

Model	Parameter	AA1	AA2	AA3	AA4
Langmuir	q_{max} (mg/g)	39.5	45.8	71.8	119.2
	b (L/mg)	0.039	0.036	0.022	0.019
	R_L^2	0.992	0.996	0.997	0.999
Freundlich	K_F	5.536	5.556	5.473	7.716
	n	2.711	2.590	2.169	2.057
	R_F^2	0.979	0.984	0.952	0.964

is formed by the stacking of irregular flake-like particles. The gap between the particles is around 100 nm, which is due to the capillary force generated when the liquid in the pores of the wet gel evaporates. Under the action of these capillary forces, the skeleton inside the wet gel collapsed, destroying the original nano network structure [36]. Unlike AA1, sample AA2 exhibits a relatively uniform structure composed of spherical particles and some flake-like particles (see Fig. 3b). The AA obtained by supercritical drying

presents a uniform structure and a three-dimensional network structure composed of nanoparticles. This is due to the supercritical drying effectively avoiding the capillary forces that usually appeared during the solvent evaporation process, resulting in low shrinkage of the skeleton and a highly porous nanostructure [35]. Some clusters can be observed on the surface of sample AA3 that was dried by supercritical carbon dioxide drying, whereas almost no clusters can be resolved on sample AA4 that was dried by ethanol supercritical drying (see Fig. 3c, d) [37]. Comparatively, the pore size of AAs obtained by supercritical drying is smaller, which is consistent with the pore-size distribution analysis results. The SEM and pore-size distribution characterization confirm that supercritical drying can effectively inhibit the aggregation of alumina particles during the drying process.

3.2 Fluoride ion adsorption performance

As shown in Fig. 4a, all the adsorption isotherms of fluoride ion for AA samples are well described by the Freundlich formula and Langmuir formula (the fitting correlation

coefficients (R^2) of all samples are larger than 95%), which suggests that both single-layer adsorption and multilayer adsorption occur in the fluoride ion adsorption process of AA [27]. However, it is evident that all the adsorption isotherms are in better agreement with the Langmuir model than the Freundlich model, which indicates a mono-layer dominated adsorption. The relevant adsorption isotherm parameters are listed in Table 3. As illustrated in Fig. 4b, all the F^- adsorption kinetic data of AA samples are well described by pseudo-first-order and pseudo-second-order models, which suggests that both chemical and physical adsorption occur in the uptake of F^- on AA. The fitted constants using the pseudo-first-order and second-order kinetic models are presented in Table 4.

The maximum F^- adsorption capacity is calculated from Langmuir model and given in Table 5. It is evident that the adsorption capacity of AA samples is positively correlated with their specific surface area and pore volume. This is due to the fact that the active sites inside the AA are more developed in the samples with higher specific surface area and pore volume, and thus providing more opportunities for fluoride ions to contact and bond.

Table 4 Kinetic parameters for F^- adsorption of AA samples

Model	Parameter	AA1	AA2	AA3	AA4
pseudo-first-order model	C_0 (mg/L)	38	38	38	38
	$Q_{e,exp}$ (mg/g)	23.33	27.33	33.33	44.67
	$Q_{e,cal}$ (mg/g)	23.48	26.87	32.71	43.38
$\ln(Q_e - Q_t) = \ln Q_e - k_1 t$	K_1 (min^{-1})	0.047	0.052	0.026	0.022
	R^2	0.995	0.964	0.876	0.812
pseudo-second-order model	$Q_{e,cal}$ (mg/g)	25.01	29.06	33.08	42.73
$t/Q_t = 1/k_2 Q_e^2 + t/Q_e$	K_2 (g/mg/min)	0.0027	0.0036	0.0024	0.0022
	R^2	0.967	0.989	0.933	0.925

Table 5 Fluoride adsorption capacity of different AA samples

Adsorbent	Temperature ($^{\circ}\text{C}$)	pH	Capacity (mg/g)	Reference
Magnetic alumina aerogel	25	5	32.1	[27]
Amorphous alumina supported carbon nano tubes	30	6	28.5	[38]
Al (III) modified calcium hydroxyapatite	15	7	26.9	[21]
Nano- Al_2O_3	25	6	14	[39]
Alum-impregnated activated alumina	25	6.5	40.6	[40]
Aluminum impregnated chitosan	25	6.5	1.7	[41]
Nano magnesium aluminum mixed oxide	25	6	10.0	[42]
AA1	25	5	39.5	Present work
AA2	25	5	45.8	
AA3	25	5	71.8	
AA4	25	5	119.2	

The maximum adsorption capacity of AA samples of our work can reach 119.2 mg/g, which is much higher than the previously reported data [21, 27, 38–42]. These results demonstrate that the supercritical drying process is an effective method for enhancing the fluoride ion adsorption performance of AA.

3.3 Mechanism for fluoride ion adsorption of AA

To ascertain the influence of fluoride ion adsorption on AA, the AA4 sample before and after adsorption of fluoride ions were characterized with XRD and EDS. AA4 after uptake of F^- from solutions with concentrations of 38 and 190 mg/L are named as AF1 and AF2, respectively. As shown in Fig. 5a, the diffraction characteristic peaks at $2\theta = 37.7, 45.9, \text{ and } 67^{\circ}$ of AF1 and AF2 indicates that the $\gamma\text{-Al}_2\text{O}_3$ crystal phase of the sample remain unchanged after the adsorption of fluoride ions. However, sharp diffraction peaks at $2\theta = 18.8, 20.2, 27.8, 40.7, \text{ and } 53.3^{\circ}$ appear in AF1 and AF2, which corresponds to the diffraction peaks of $\text{Al}(\text{OH})_3$ (001), (110), (111), (131), and (132) crystal planes (PDF no.74-1119), respectively. This is due to the fact that the AA is protonated to form Al–OH bonds in an acidic aqueous solution, and the generated –OH bonds will be easily replaced by F^- . EDS element mapping results shown in Fig. 5b gives a clear picture of the F element distribution in the samples. F is uniformly distributed within the sample, which also confirms the adsorption of F^- in AA4.

Due to its intrinsic lattice defects and unique pore structure, AA possesses excellent adsorption capacity. The kinetic experiments have confirmed both physical and chemical adsorption of fluoride ions in AA. The pore-size distribution and the fluoride ion adsorption data illustrate that the fluoride ion adsorption capacity of AA is correlated with its specific surface area and mesoporous structure. The mechanism of fluoride adsorption in AA is shown in Fig. 6. Under acidic conditions ($\text{pH} < 6$),

Fig. 5 **a** XRD pattern of AA4 before and after F^- adsorption; **b** EDS element mapping of AA4 after F^- adsorption

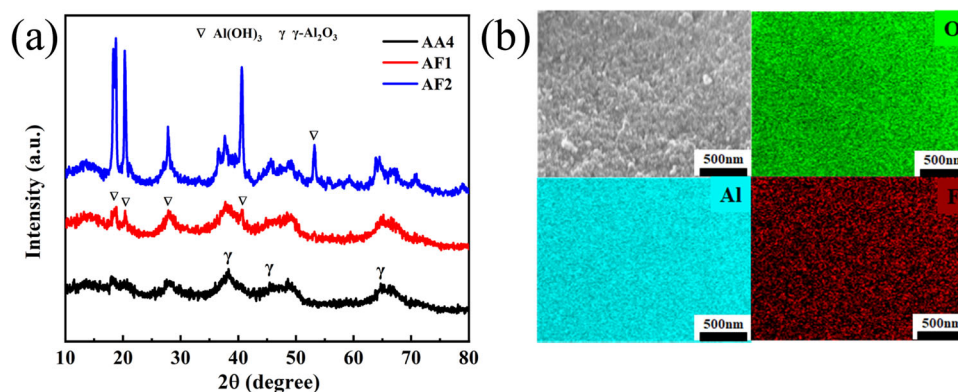
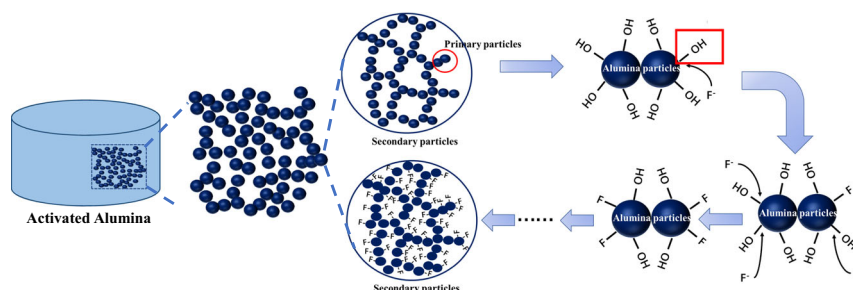
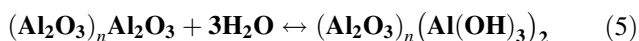


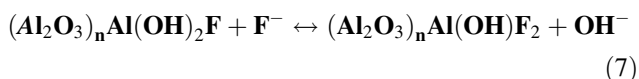
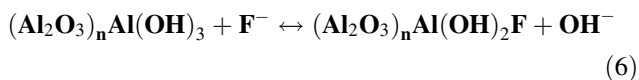
Fig. 6 Fluoride ion adsorption schematic of AA



the surface of alumina will react as follows:



In a solution containing fluoride ions, free fluoride ions will replace the hydroxyl groups on aluminum hydroxide, thereby adsorbing the fluoride ions [14, 27]. The adsorption process will continue until the adsorption is saturated (usually it takes 48 h). The complex reaction of ions on the surface of AA are as follows:



As shown in Fig. 6, supercritical dried AA possesses an ultra-high specific surface area and a well-developed internal pore structure, which greatly increases the number of internal active sites. Supercritical dried AA is composed of primary particles and secondary particles formed by the aggregation of the primary particles. In an acidic solution, the surface functional groups on these particles will be gradually replaced by fluoride ions during the adsorption progress. Fluoride ions can easily enter into the pores of AA and react with the alumina

particles. Therefore, the overall adsorption performance of the highly porous AA prepared by the supercritical drying method is greatly improved.

4 Conclusions

Highly porous AA with excellent fluoride removal performance was successfully prepared by a sol–gel method coupled with supercritical drying. Supercritical drying plays a crucial role in the preparation of the AA, which provides AA with a unique pore structure. The resultant AAs show ultra-high specific surface area of $660 \text{ m}^2/\text{g}$, large pore volume of $4.03 \text{ cm}^3/\text{g}$ and uniform three-dimensional network nanostructure, which contributes to the combination of fluoride ions and alumina particles inside AA. The fluoride ion adsorption capacity is greatly improved (119.2 mg/g) compared to that of more conventional AAs previously reported.

Acknowledgements This work was financially supported by National Key Research and Development Program of China (2017YFA0204600) and National Natural Science Foundation of China (11874288).

Compliance with ethical standards

Conflict of interest The authors declare no competing interests.

Publisher's note Springer Nature remains neutral with regard to jurisdictional claims in published maps and institutional affiliations.

References

1. Fordyce FM (2019) Fluorine: human health risks. In: Nriagu J (ed) Encyclopedia of environmental health, 2nd edn. Elsevier, Amsterdam
2. Amini M, Mueller K, Abbaspour KC, Rosenberg T, Afyuni M, Møller KN, Sarr M, Johnson CA (2008) Statistical modeling of global geogenic fluoride contamination in groundwaters. *Environ Sci Technol* 42:3662–3668
3. Reddy NB, Prasad KSS (2003) Pyroclastic fluoride in ground waters in some parts of Tadpatri Taluk, Anantapur district, Andhra Pradesh. *Indian J Environ Health* 45(4):285–288
4. Nell JA, Livanos G (1988) Effects of fluoride concentration in seawater on growth and fluoride accumulation by Sydney rock oyster (*Saccostrea commercialis*) and flat oyster (*Ostrea angasi*) spat. *Water Res* 22:749–753
5. Bhatnagar A, Kumar E, Sillanp M (2011) Fluoride removal from water by adsorption—A review. *Chem Eng J* 171:811–840
6. Won CH, Choi J, Chung J (2012) Evaluation of optimal reuse system for hydrofluoric acid wastewater. *J Hazard Mater* 239:110–117
7. Singh K, Lataye DH, Wasewar KL, Yoo CK (2013) Removal of fluoride from aqueous solution: status and techniques. *Desalin Water Treat* 51:3233–3247
8. Shen J, Mkongo G, Abbt-Braun G, Ceppi SL, Richards BS, Schäfer AI (2015) Renewable energy powered membrane technology: Fluoride removal in a rural community in northern Tanzania. *Sep Purif Technol* 149:349–361
9. Kabay N, Arar O, Samatya S, Yueksel U, Yueksel M (2008) Separation of fluoride from aqueous solution by electro dialysis: effect of process parameters and other ionic species. *J Hazard Mater* 153:107–113
10. Biswas K, Gupta K, Goswami A, Ghosh UC (2010) Fluoride removal efficiency from aqueous solution by synthetic iron (III)–aluminum(III)–chromium(III) ternary mixed oxide. *Desalination* 255:44–51
11. Sehn P (2008) Fluoride removal with extra low energy reverse osmosis membranes: three years of large scale field experience in Finland. *Desalination* 223:73–84
12. Shen J, Schaefer AI (2015) Factors affecting fluoride and natural organic matter (NOM) removal from natural waters in Tanzania by nanofiltration/reverse osmosis. *Sci Total Environ* 527:520–529
13. Kundu S, Chowdhury IH, Sinha PK, Naskar MK (2017) Effect of organic acid-modified mesoporous alumina toward fluoride ions removal from water. *J Chem Eng Data* 62:2067–2074
14. Lin J, Chen Y, Hong X, Huang C, Huang CP (2020) The role of fluoroaluminate complexes on the adsorption of fluoride onto hydrous alumina in aqueous solutions. *J Colloid Interface Sci* 561:275–286
15. Hao OJ, Huang CP (1986) Adsorption characteristics of fluoride onto hydrous alumina. *J Environ Eng* 112:1054–1069
16. Kim Y, Kim C, Choi I, Rengaraj S, Yi J (2004) Arsenic removal using mesoporous alumina prepared via a templating method. *Environ Sci Technol* 38:924–931
17. Xu N, Liu Z, Dong Y, Hong T, Dang L, Li W (2016) Controllable synthesis of mesoporous alumina with large surface area for high and fast fluoride removal. *Ceram Int* 42(14):15253–15260
18. Camacho LM, Torres A, Saha D, Deng S (2010) Adsorption equilibrium and kinetics of fluoride on sol–gel-derived activated alumina adsorbents. *J Colloid Interface Sci* 349(1):307–313
19. Rafique A, Awan MA, Wasti A, Qazi IA, Arshad M (2013) Removal of fluoride from drinking water using modified immobilized activated alumina. *J Chem* 2013:386476
20. Ekka B, Dhaka RS, Patel RK, Dash P (2017) Fluoride removal in waters using ionic liquid-functionalized alumina as a novel adsorbent. *J Clean Prod* 151:303–318
21. Nie Y, Hu C, Kong C (2012) Enhanced fluoride adsorption using Al (III) modified calcium hydroxyapatite. *J Hazard Mater* 233–234:194–199
22. Chang CF, Lin PH, Höll W (2006) Aluminum-type superparamagnetic adsorbents: synthesis and application on fluoride removal. *Colloids Surf A: Physicochemical Eng Asp* 280(1–3):194–202
23. Zhao X, Wang J, Wu F, Wang T, Cai Y, Shi Y, Jiang G (2010) Removal of fluoride from aqueous media by Fe₃O₄@Al(OH)₃ magnetic nanoparticles. *J Hazard Mater* 173:102–109
24. Li Y, Gan K, Huo W, Liu K, Liu J, Wang X, Yu H, Yang J (2019) Novel design of high-surface-area poly-hollow alumina spheres via a facile ball dropping method based on particle-stabilized emulsions. *Ceram Int* 45(17):22940–22947
25. Shi Z, Jiao W, Chen L, Wu P, Wang Y, He M (2016) Clean synthesis of hierarchically structured boehmite and γ -alumina with a flower-like morphology. *Microporous Mesoporous Mater* 224:253–261
26. Zhu XH, Yang CX, Yan XP (2018) Metal-organic framework-801 for efficient removal of fluoride from water. *Microporous Mesoporous Mater* 259:163–170
27. Yang W, Dou X, Li Y, Mohan D, Pittman CU, Ok YS (2016) Performance and mass transfer of aqueous fluoride removal by a magnetic alumina aerogel. *RSC Adv* 6:112988–112999
28. Zou W, Wang X, Wu Y, Zu G, Zou L, Zhang R, Yao X, Shen J (2017) Highly thermally stable alumina-based aerogels modified by partially hydrolyzed aluminum tri-sec-butoxide. *J Sol-Gel Sci Technol* 84:507–514
29. Zu G, Shen J, Zou L, Wang W, Lian Y, Zhang Z, Du A (2013) Nanoengineering super heat-resistant, strong alumina aerogels. *Chem Mater* 25:4757–4764
30. Yu H, Jiang Y, Lu Y, Li X, Zhao H, Ji Y, Wang M (2019) Quartz fiber reinforced Al₂O₃-SiO₂ aerogel composite with highly thermal stability by ambient pressure drying. *J Non-Crystalline Solids* 505:79–86
31. Wu X, Shao G, Shen X, Cui S, Wang L (2016) Novel Al₂O₃-SiO₂ composite aerogels with high specific surface area at elevated temperatures with different alumina/silica molar ratios prepared by a non-alkoxide sol–gel method. *Rsc Adv* 6:5611–5620
32. Boumaza A, Favaro L, Lédion J, Sattonnay G, Brubach JB, Berthet P, Huntz AM, Roy P, Tétot R (2009) Transition alumina phases induced by heat treatment of boehmite: An X-ray diffraction and infrared spectroscopy study. *J Solid State Chem* 182:1171–1176
33. Sing KSW (1985) Reporting physisorption data for gas/solid systems with special reference to the determination of surface area and porosity (Recommendations 1984). *Pure Appl Chem* 57(4):603–619
34. Hüsing N, Schubert U (2010) Aerogels—airy materials: chemistry, structure, and properties. *Angew Chem Int Ed* 37:23–45
35. Lázár I, Fábíán I (2016) A continuous extraction and pumpless supercritical CO₂ drying system for laboratory-scale aerogel production. *Gels* 2(4):26
36. Brinker CJ, Scherer GW (2013) Sol-gel science: the physics and chemistry of sol-gel processing. Academic press, Boston
37. Baumann TF, Gash AE, Chinn SC, Sawvel AM, Maxwell RS, Satcher JH (2005) Synthesis of high-surface-area alumina aerogels without the use of alkoxide precursors. *Chem Mater* 17:395–401
38. Li YH, Wang S, Cao A, Dan Z, Zhang X, Xu C, Luan Z, Ruan D, Liang J, Wu D, Wei B (2001) Adsorption of fluoride from water by amorphous alumina supported on carbon nanotubes. *Chem Phys Lett* 350:412–416

39. Kumar E, Bhatnagar A, Kumar U, Sillanpaa M (2011) Defluoridation from aqueous solutions by nano-alumina: characterization and sorption studies. *J Hazard Mater* 186:1042–1049
40. Tripathy SS, Bersillon J, Gopal K (2006) Removal of fluoride from drinking water by adsorption onto alum-impregnated activated alumina. *Sep Purif Technol* 50:310–317
41. Swain SK, Dey RK, Islam M, Patel RK, Jha U, Patnaik T, Airoidi C (2009) Removal of fluoride from aqueous solution using aluminum-impregnated chitosan biopolymer. *Sep Sci Technol* 44:2096–2116
42. Shukla R, Ramkumar J, Tyagi AK (2010) Nanocrystalline magnesia alumina mixed oxide: efficient defluoridation sorbent. *Int J Nanotechnol* 7:989–1002